

PIV investigation of flow behind a permeable rib turbulator

P. K. PANIGRAHI, A. SCHRODER, J. KOMPENHANS
Institute of Aerodynamics and Flow Technology
German Aerospace Center
Bunsenstrasse 10, Goettingen
GERMANY

<http://home.iitk.ac.in/~panig>, http://www.dlr.de/as/institut/abteilungen/abt_ev

Abstract: - The interaction between the primary and secondary vortices behind a permeable rib turbulator have potential for many practical applications with specific benefit to heat transfer augmentation, mixing enhancement and drag reduction. When the primary vortices are stretched by the orthogonally oriented secondary vortices, there is a possibility of the fluid forces diminishing while the additional vorticity in the fluid can continue to enhance heat transfer and mixing effectiveness. The additional secondary vortices are generated by flow through the perforation of the permeable rib turbulator. The flow through the slit is expected to generate additional secondary vortices which can lead to subharmonic growth through vortex merging. The presence of an obstruction through the slit, termed here as splitter can lead to the generation of streamwise vorticity. This streamwise vorticity can stretch the spanwise vorticity of the flow leading to the net modulation of the vorticity field. In addition, the base flow in the near wall and the wake region is modified with possibility for simultaneous reduction of pressure penalty and mixing enhancement. The flow behind the turbulator is three dimensional and time dependent. Therefore, mean and fluctuating 3-D velocity field statistics from stereo PIV measurements has been presented and discussed.

Key-Words: Stereo PIV, Turbulator, Turbulent flow, Mixing enhancement, Permeable rib, Vortex

Nomenclature:

X, Y, Z	Spatial coordinates
u, v, w	Mean velocity components
h	Rib height
U^+	Normalized velocity in wall coordinate
Y^+	Normalized Y in wall coordinate
U_τ	Wall shear velocity
U_∞	Free stream velocity
δ	Boundary layer thickness
δ^*	Displacement thickness
θ	Momentum thickness
ω	Vorticity
rms	Root mean square

particle image velocimetry is well suited to study the instantaneous flow structures and dynamics of the flow. Few experimental investigations related to this type of flow showing the spatio-temporal structures have been carried out and are briefly described below.

Backward facing step flow has been investigated by number of researchers as a base-line case for study of flow separation and reattachment. Kostas et al. [1] carried out particle velocity measurements (2-C PIV) on a backward facing step flow and performed the proper orthogonal decomposition of the fluctuating velocity and vorticity fields. They observed the large scales to contribute to the Reynolds stresses and turbulent kinetic energy production downstream of reattachment and small scales to contribute to the Reynolds stresses in the vicinity of reattachment. Schram et al. [2] investigated the eddy structures shed in a backward facing step flow using particle image velocimetry (2-C PIV). They implemented a vortex detection algorithm based on wavelet transform. The vortex core diameter to backward facing step height ratio is between the range of 0.08 and 0.2 and the streamwise evolution of the vortex core diameter does not exhibit significant change.

Islam et al. [3] investigated the turbulent water flow structure over micro-repeated ribs in a narrow two-dimensional rectangular channel by particle image velocimetry (2-C PIV). They observed no significant effect of the pitch and Reynolds number on the reattachment length beyond a critical value of Reynolds

1 Introduction

The use of periodic roughness element i.e. ribs, delta wings etc. to enhance the heat transfer and mixing is a well-established approach practiced in heat exchanger and cooling passage of the gas turbine blade. The flow past the roughness element leads to separation due to the sudden expansion and subsequent reattachment downstream with a recirculating region both upstream and downstream. The flow in the reattaching region is highly three dimensional and unsteady and the boundary layer begins to redevelop to a normal turbulent boundary layer state in the downstream region. Previous investigations to this complex flow have primarily used single point measurement technique i.e. hot wire anemometry, laser Doppler velocimetry and flow visualization etc. The advent of multi-dimensional

number. Callaud and David [4] investigated the 3D features of the flow around a surface-mounted block using stereoscopic particle image velocimetry. The 3D calibration was carried out based on a real linear camera model, which does not require the introduction of parameters and knowledge of the geometric configuration of the stereoscopic system in order to determine the calibration matrices. They observed the errors during the calibration step to be small compared to the bi-dimensional velocity field measurements.

Different permeable rib geometries have been proposed by various investigators and shown to be more effective than the solid rib. Huang [5] investigated the effect of interrupted slits in a rib on heat transfer of a rectangular channel using laser holographic interferometry and observed superior heat transfer performance of the slit-ribbed channel. Panigrahi and Tariq [6] investigated the heat transfer and pressure penalty behind the surface mounted slit rib with different open area ratios and observed higher heat transfer for the slit rib compared to the solid rib for open area ratio less than 30% with simultaneous reduction in pressure penalty compared to the solid rib. Tariq et al. [7] reported the detailed flow and heat transfer behind slit rib of different open area ratio using liquid crystal thermography, hot wire anemometry, cold wire anemometry and flow visualization. They showed the interaction between the reattaching flow past the rib with the flow through the slit to successfully modify the near wall and wake region mean flow and fluctuation. Panigrahi and Acharya [8] presented the coherent and random component of the turbulent energy and shear stress, the energy exchange with the mean flow and between the modes and the phase decorrelation of the coherent components. They observed the large scale structures to be significant both in the near field and far field region, while the binary energy exchange to be significant in the near field region. The excitation enhances the shear layer growth and the fundamental-subharmonic excitation does not provide any significant improvement over the fundamental excitation.

Based on the literature, no 3-C velocity field measurements behind surface mounted rib turbulator have been reported by the researchers. Also none of the 2-C planar velocity field measurements have reported the velocity field in the cross-flow plane and the associated ω_x vorticity. The axial vorticity (ω_x) is predominant in delta wing type of rib turbulator, while the spanwise vorticity (ω_z) is strong in the rib type turbulator. The geometric modification i.e. introduction of slit and splitter in a solid rib (Fig. 2) proposed in this work is expected to combine the beneficial effect of both the delta-wing and solid rib types of turbulator. The axial vorticity is expected to be significant for the permeable

rib turbulator due to the presence of splitter inside the slit. Therefore, this work reports the 3-C mean and fluctuating velocity field measurements of permeable rib along with the ω_x vorticity and compares with the solid rib counterpart.

2 Experimental Setup

The experiments have been carried out in the low turbulence wind tunnel of DLR Gottingen (Fig. 1). The test section is of $0.3\text{m} \times 1.5\text{m}$ cross section and 6.25 meter long. The air enters through a contraction cone (contraction ratio, 16:1), settling chamber of $5\text{m} \times 1.5\text{m}$ cross section and anti-turbulence screens. The average turbulence intensity of the wind tunnel is about 0.05%. A flat plate (Fig. 2) with a 6:1 elliptical leading edge (to prevent large scale boundary layer separation at the leading edge), 300 mm wide and 1180 mm long has been mounted between the side walls of the wind tunnel as a test model. One sand paper of 10 mm wide has been mounted at the leading edge of the flat plate and a second sand paper of 20 mm wide has been mounted at a streamwise distance of 140 mm from the leading edge of the flat plate. A glass window has been mounted at the central bottom portion of the flat plate for the access of the laser light sheet from below. The wooden portion of the flat plate and the remaining portion of the test section have been painted with black paint to minimize the noise due to the reflection of laser light.

Different rib turbulator geometries studied in this work have been presented in Fig. 2. The ribs are square cross section of 14×14 mm. The slit thickness is equal to 3 mm leading to an open area ratio (ratio of the projected dimension of the slit to that of the rib) of the slit rib equal to 20%. A splitter of 28×3 mm cross section is introduced at the center of the slit for the split-slit rib.

A laskin nozzle has been used to introduce the seeding (diethylhexylsebakat (DEHS)) at the entrance of the settling chamber. The mean tracer particle size is $1\ \mu\text{m}$ (Kahler et al. [9]). The seeding generator is switched off during the data acquisition to prevent any effect of external disturbance due to the blowing of the compressed air through the seeding generator. The seeding density is mostly sufficient after running the seed generator for few minutes due to the recirculation of room air. The online display of the particle images helps in guiding the quality of seeding density during the image acquisition.

The Nd:YAG laser system (Quantel, Les Ulis, France) with an output energy of 300 mJ per pulse at wavelength, $\lambda = 532$ nm has been used as light source. One biconcave lens ($f=150\text{mm}$), one biconvex lens ($f=300\text{mm}$), one cylindrical lens ($f=40\text{mm}$) and four

mirrors have been used to generate about 2mm thick and 150 mm wide light sheet. The synchronization between the laser light pulse and the camera has been accomplished by the TTL pulse from the synchronizer. The cylindrical lens and the mirror positions are adjusted for controlling the light sheet position and its orientation with respect to the mean flow (stream wise or spanwise). Two PCO Sensicam camera (Kelheim, Germany) of 1280×1024 pixel with Zeiss (Jena, Germany) Makro Planar objectives (f-number = 2.8, f=100 mm) have been used for image acquisition. The time separation between the two laser pulses is varied in the range of 60–90 sec. The frequency of image pair acquisition is 3.3 Hz. For the calculation of the mean velocity field statistics, 1000 number of image pairs have been acquired.

The raw PIV images have been pre-processed with a high pass filter (kernel size = 5 pixel) prior to the PIV cross-correlation calculation. The interrogation window size is 32×32 pixel² with overlapping of 62%. The resolution in both X and Y direction is equal to 0.86 mm. The average particle image displacement for the PIV images is about 4 pixels. The Whitaker sub-pixel peak fit algorithm has been used to reduce the peak-locking effect during the fractional displacement estimation. Multi-grid correlation from an initial grid size of 96×96 to 32×32 pixel have been implemented with sub-pixel image shifting (B-Spline interpolation) from the initial to final grid size. The average number of spurious vectors (based on maximum image displacement equal to 5 pixel) is about 1.1 % and the correlation coefficient being between 0.3 and 0.9 indicate high quality of the PIV recordings.

The stereo PIV has been configured based on the angular lens displacement with tilted back plane (Scheimpflug condition). The calibration grid images from both the cameras have been reconstructed to the object plane based on back-projection algorithm. The reconstructed coefficients for each camera are used subsequently for the calculation of the planar velocity field for the respective camera. The 3-C velocity field has been determined from the two planar velocity fields on the basis of perspective projection assuming geometric imaging.

3 Results and discussions

3.1 PIV implementation

The stereo PIV measurements require two sets of calibration images of the calibration grid located at the light sheet position. The two planar field measurements based on these two separate calibration coefficients are combined subsequently to calculate all three velocity components. It is essential that the calibration grid and the light sheet plane are perfectly aligned in the measurement region. But, it is not always feasible to

have perfect alignment and therefore residual alignment is carried out between the two raw images of both the left and right camera to correct the calibration coefficients. The error in the back-propagation calculation, the error in Scheimpflug adjustment and the camera noise add to the uncertainty in the velocity field calculation. To assess the accuracy of the PIV implementation, the stereo PIV measurement has also been repeated with 2-C PIV technique. The stereo PIV measurements have been acquired with the light sheet aligned both in streamwise (X - Y) and spanwise (Y - Z) plan. The mean and RMS u -velocity from the 2-C and 3-C PIV techniques have been compared in Fig. 3. The mean velocity field shows a perfect match between 2-C and 3-C PIV implementation. The rms velocity in Fig. 3 also has a reasonable match between different PIV implementation considering the higher uncertainty in the fluctuating field measurements. Hence, it can be concluded that the stereo PIV technique has been properly implemented in this work.

3.2 Incoming flow

The smooth wall flow at the streamwise X -location where the rib is mounted has been compared with the turbulent universal boundary layer profile in Fig. 4. The reasonable match between the two indicates the turbulent nature of the incoming flow approaching the surface mounted rib. The properties of this incoming flow boundary layer have been compiled in Table 1. The surface mounted rib is submerged inside the incoming turbulent boundary layer of shape factor 1.6. The Reynolds number based on the momentum thickness of the incoming boundary layer and the rib height is equal to 695 and 5538 respectively.

3.3 Mean flow

The mean flow vector field (v, w) and the u -component of velocity at $X/h=3$ and 5 location have been shown in Fig. 5 and Fig. 6 respectively. At $X/h=3$, the u -velocity shows no strong spanwise variation in the Z -direction for the solid rib. However, there is small variation of the u -velocity in the spanwise direction for the slit rib and strong spanwise variation for the split-slit rib due to the presence of the splitter. The cross stream extent of the split-slit rib recirculation zone is maximum behind the splitter. The symmetry of the v and w velocity variation around the splitter region is also evident in Fig 5. The recirculation zone extends to a larger extent in the cross-stream (Y) direction for the solid rib in comparison to the slit rib and split-slit rib indicating larger reattachment length for the solid rib. The ω_x vorticity field in Fig. 5 shows distinct difference in the size (based on the size of the iso-vorticity contour) and strength of eddies for different rib turbulators. For the split-slit rib turbulator, there are two distinct zones of opposite vorticity around the splitter region. Uniform

patterns of vorticity contours in the mid shear layer region ($Y/h=1$) are observed for the slit rib, which may be attributed to the instability of flow through the slit. The size of the vorticity contour for the solid rib is larger than the slit rib and is the result of the three dimensional separation.

The Fig. 6 shows strong negative recirculating velocity for the solid rib contrast to the slit rib and split-slit rib. This indicates the delay in reattachment of the solid rib in comparison to the solid rib. The spanwise variation of the u -velocity shows larger variation for the slit rib at $X/h=5$ compared to that at $X/h=3$ indicating higher three dimensionality at the former streamwise location. The strength of the recirculating zone behind the splitter has considerably diminished for the split-slit rib at $X/h=5$ location compared to the earlier location ($X/h=3$). Stronger three dimensionality for the permeable rib is also manifested by the larger v and w velocity magnitude variation at $X/h=5$ compared to that at $X/h=3$. The iso-contour of vorticity in Fig. 6 shows clear difference between the solid and permeable rib in the near wall region and the edge of the shear layer. However, the vorticity contour in the shear layer region show similar variation for solid and permeable ribs. The geometrical modification of the rib turbulator is predominantly effective on the near wall structures in the far field region.

3.4 Fluctuating flow

The normal stress (u_{rms} , v_{rms} and w_{rms}) variation for different rib turbulators at $X/h=3$ and 5 location have been compared in Fig. 7 and Fig. 8 respectively. The v_{rms} fluctuation has the lowest magnitude and w_{rms} has the highest magnitude for both solid and permeable ribs. The nature of variation of the rms velocity in Fig. 7 and Fig. 8 is similar to the respective u -velocity variation in Fig. 5 and Fig. 6. This indicates the larger role played by the streamwise velocity gradient in the turbulent kinetic energy production. The clear downward movement of the maximum magnitude of the rms velocity from $X/h=3$ location (Fig. 7) to $X/h=5$ location (Fig. 8) for the permeable rib compared to the solid rib confirms to the earlier reattachment of the permeable rib. The average magnitude of the rms fluctuation is highest for the solid rib and lowest for the permeable rib. However, the permeable ribs show shorter reattachment length and higher three dimensionality. This is an indication of superior performance of the permeable ribs for mixing and heat transfer enhancement in comparison to the solid rib.

3.5 Instantaneous flow

The instantaneous u -velocity field at 0.3 sec time interval for different rib turbulators has been compared in Fig. 9. The near wall flow structures show high

temporal variation and are function of the rib geometry. The near wall negative velocity fluid packet has a larger cross stream (Y) extent for the solid rib in comparison to the permeable rib. The negative velocity fluid packet shows more discontinuous motion in the spanwise direction for the solid rib and the split-slit rib contrary to the slit rib. The presence of the splitter is responsible for the discontinuity of the spanwise motion for the split-slit rib. The size of the shear layer zone also shows temporal variation for all rib turbulators. This interesting spanwise temporal variation of the recirculating bubble in Fig. 9 behavior is not evident from the mean and fluctuating velocity statistics in Figs. 5 -8.

4 Conclusion

The following important conclusions can be drawn from the stereo-PIV measurements of solid and permeable ribs.

- The permeable ribs have a shorter reattachment length compared to the solid rib.
- The flow past the permeable rib approach to 3-dimensionality earlier than the solid rib.
- The splitter inside the slit has a strong influence on the mean and fluctuating velocity field in the near field region.
- The instantaneous flow field indicates a spanwise oscillation of the recirculating bubble in the near wall region, which is function of the rib geometry.

ACKNOWLEDGMENTS

The authors gratefully acknowledge the Alexander von Humboldt Foundation (<http://www.humboldt-foundation.de>) for the support.

References:

- [1] J. Kostas, J. Soria, M. S. Chong, Particle velocimetry measurements of a backward-facing step flow, *Experiments in Fluids*, Vol. 33, 2002, pp. 838-853.
- [2] C. Schram, P. Rambaud, M. L. Riethmuller, Wavelet based eddy structure eduction from a backward facing step flow investigated using particle image velocimetry, *Experiments in Fluids*, Vol. 36, 2004, pp. 233-245.
- [3] M. Shafiqul Islam, K. Haga, M. Kaminaga, R. Hino, M. Monde, Experimental analysis of turbulent flow structure in a fully developed rib-roughened rectangular channel with PIV, *Experiments in Fluids*, Vol. 33, 2002, pp. 296-306.
- [4] D. Callaud, L. David, Stereoscopic particle velocimetry measurements of the flow around a surface-mounted block, *Experiments in Fluids*, Vol. 36, 2004, pp. 53-61
- [5] J. J. Hwang, Heat transfer-friction characteristic comparison in rectangular ducts with slit and solid

ribs mounted on one wall, *ASME J. Heat Transfer*, Vol. 120, 1998, pp. 709-716.

- [6] P. K. Panigrahi, A. Tariq, Liquid crystal heat transfer measurements in a rectangular channel with solid and slit rib, *J. Flow Visualization*, Vol. 6, 2003, pp. 407-416.
- [7] Andallib Tariq, P. K. Panigrahi, K. Muralidhar, Flow and heat transfer in the wake of a surface mounted rib with a slit, *Experiments in Fluids*, 2004, In Press.
- [8] P. K. Panigrahi, S. Acharya, Multi-modal forcing of the turbulent separated flow past a rib, *ASME J. Fluids Engineering*, Vol. 126, 2004, pp. 22-31.
- [9] C. J. Kahler, B. Sammler and J. Kompenhans, Generation and control of tracer particles for optical flow investigations in air, *Experiments in Fluids*, Vol. 33, 2002, pp. 736-742.

Table 1 The boundary layer properties at the streamwise location where the rib is mounted.

δ [mm]	δ^* [mm]	θ [mm]	u_τ [m/s]	u_∞ [m/s]
15.3	2.86	1.758	0.29	5.8

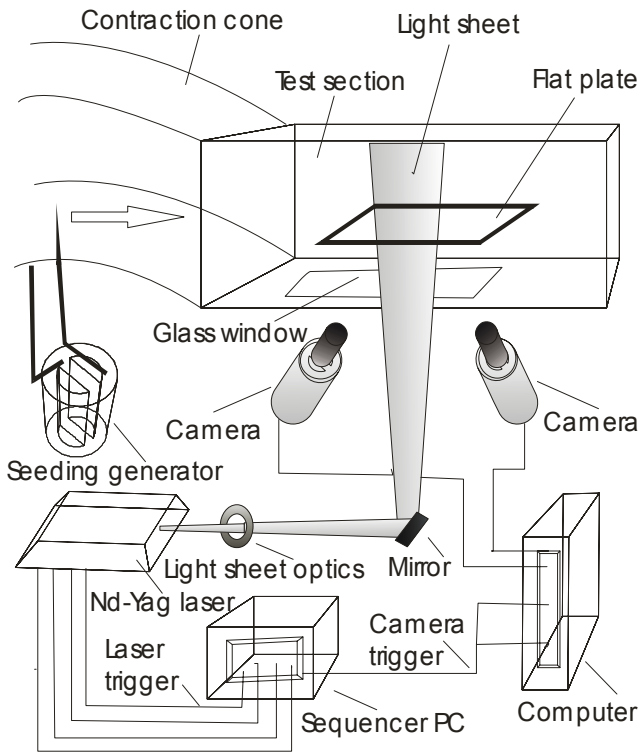


Fig. 1 The sketch of the experimental setup.

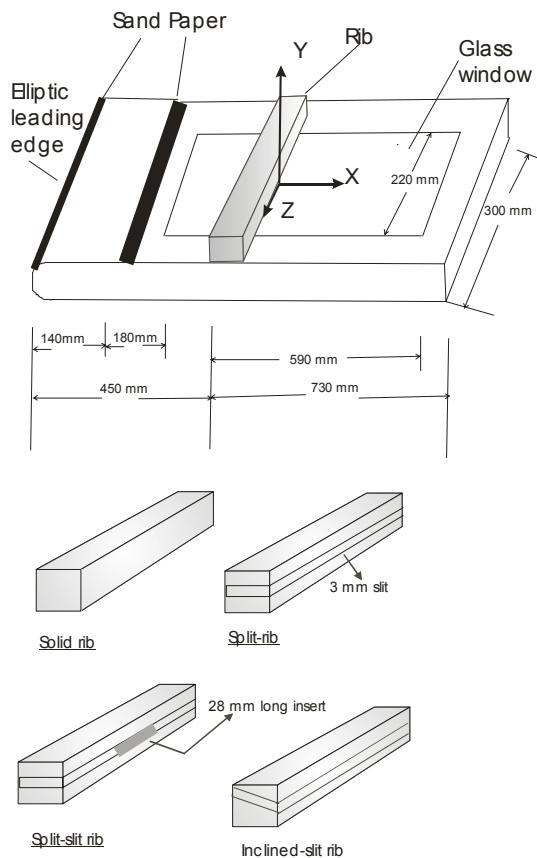


Fig. 2 The sketch of the flat plate, coordinate system and different rib turbulator geometries.

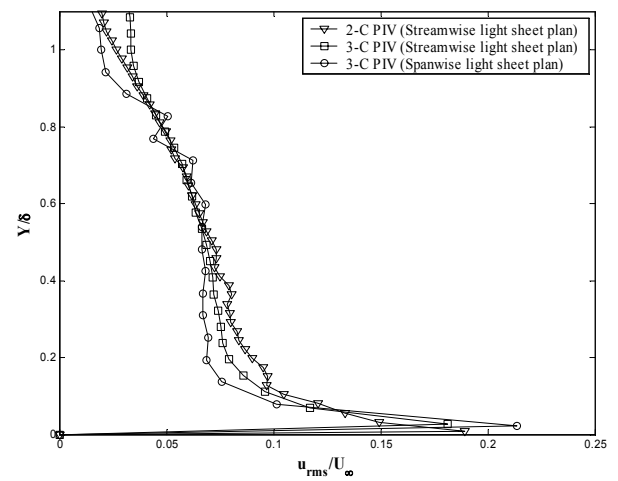
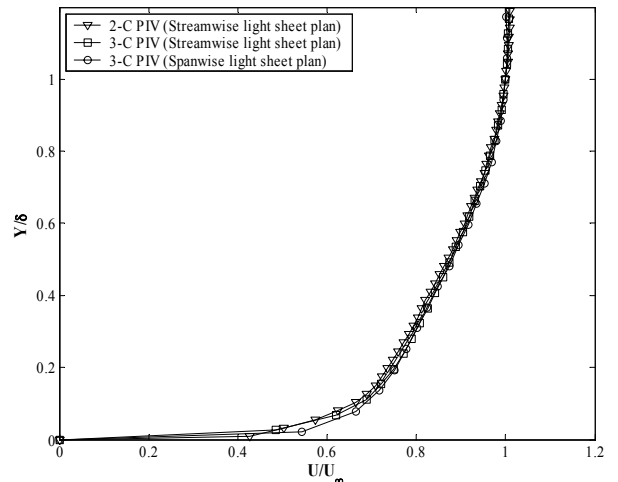


Fig. 3 The mean (top) and rms (bottom) u-velocity comparison for different implementation of the PIV technique i.e. 2-C PIV, 3-C PIV with laser light sheet in streamwise plane and spanwise plane.

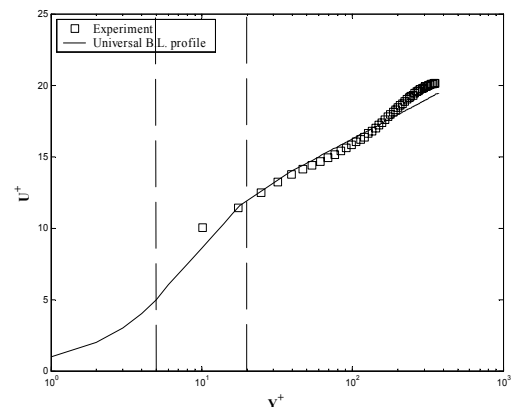


Fig. 4 The smooth-wall boundary layer profile in wall coordinate, where the rib is mounted. The universal B.L. profile, $U^+ = Y^+$ ($Y^+ < 5$), $U^+ = 5.0 Y^+ - 2.9$ ($Y^+ < 20$) and $U^+ = 2.44 \ln Y^+ + 5.0$ have been superimposed for comparison.

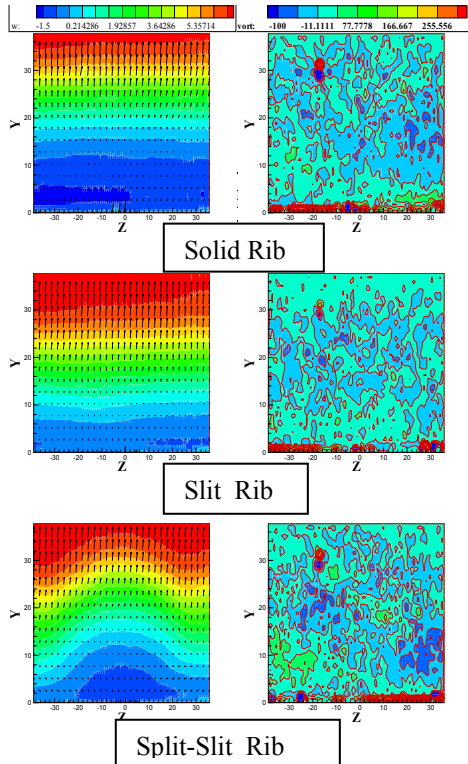


Fig. 5 The mean velocity (v, w) vector field superposed on the contour of the u -velocity (left) and the ω_x vorticity contour (right) at the spanwise plane ($X/h = 3$) for different rib turbulators.

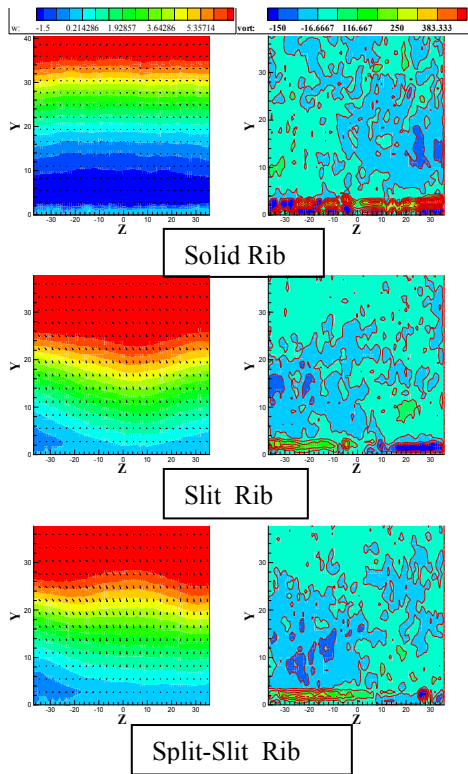


Fig. 6 The mean velocity (v, w) vector field superposed on the contour of the u -velocity (left) and the ω_x vorticity contour (right) at the spanwise plane ($X/h = 5$) for different rib turbulators.

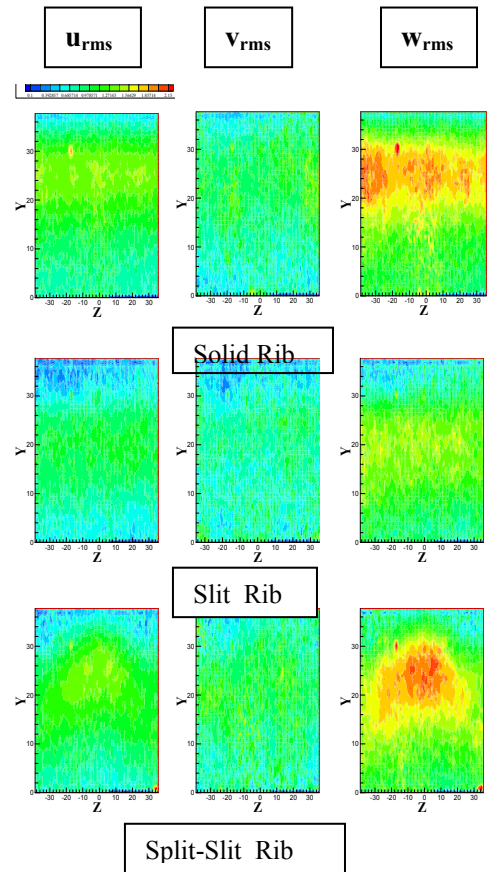


Fig. 7 The normal stresses at the spanwise plane ($X/h = 3$) for different rib turbulators.

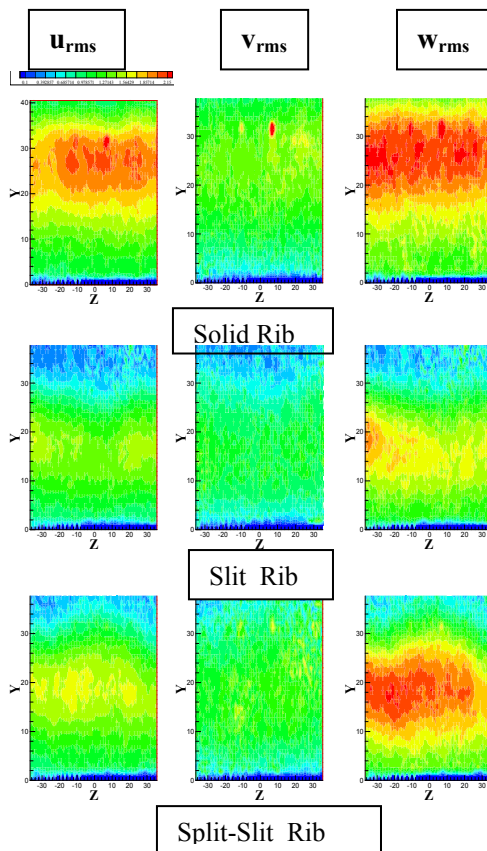


Fig. 8 The normal stresses at the spanwise plane ($X/h = 5$) for different rib turbulators.

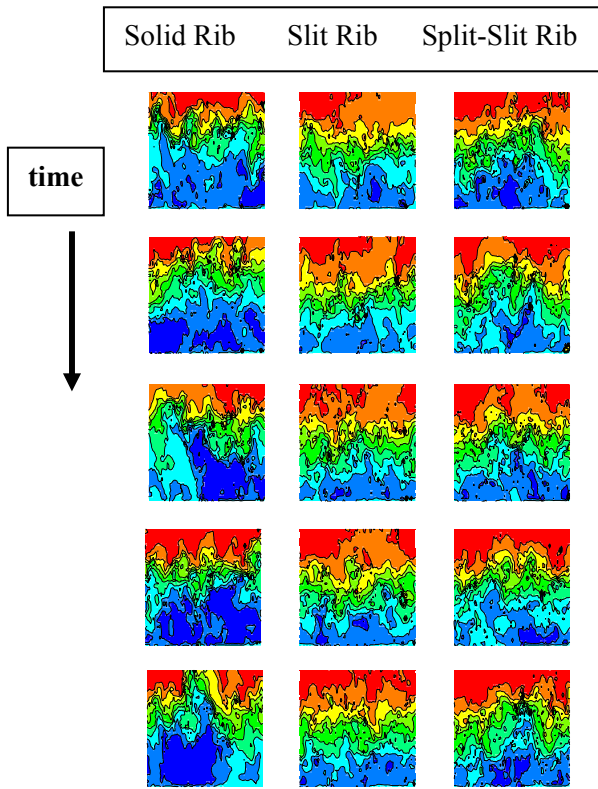


Fig. 9 The instantaneous streamwise velocity (u) at $X/h = 3$ location with 0.3 second time interval for different rib turbulators.